Coherent-potential and average t-matrix approximations for disordered muffin-tin alloys. II. Application to realistic systems

A. Bansil
Department of Physics, Northeastern University, Boston, Massachusetts 02115
(Received 28 November 1978)

In an earlier article, the electronic spectrum of the disordered alloy A_xB_{1-x}, using the coherent-potential (CPA) and the average t-matrix (ATA) approximations, was discussed within the framework of the muffin-tin Hamiltonian. Using the illustrative examples of Cu_xNi_{1-x} and Cu_xZn_{1-x}, the present paper exposes the physically relevant aspects of the electronic spectra of disordered transition and noble-metal alloys. Bloch spectral densities, complex energy bands, impurity levels, and average total and component densities of states are considered. We also discuss how the effects of transfer of charge between the constituents on their atomic potentials can be included in a semiempirical manner in the present framework.

I. INTRODUCTION

The electronic structure of disordered alloys has been the subject of many recent theoretical and experimental studies.[1-3] On the theoretical side, attention has been focused on the so-called muffin-tin Hamiltonian for a random binary alloy A_xB_{1-x}. It is well established that, in closed packed systems in general, and in perfect crystals of noble and transition metals in particular, a realistic description of the electronic structure is possible on the basis of the muffin-tin Hamiltonian. It is clear, therefore, that to obtain a comparably detailed description of alloys of transition and noble metals, the muffin-tin framework must be used.

In the preceding article,[4] the relevant formal aspects of the coherent-potential approximation (CPA) and a new version of the average t-matrix approximation (ATA), which has many advantages over the currently used form, were discussed. Our main purpose in this article is to delineate the dominant features of the alloy electronic spectrum in light of these formal developments. Since we have studied Cu_xZn_{1-x} and Cu_xNi_{1-x} before, it seemed best to use these same systems for the present illustrative purposes. In particular, the Cu, Ni, and Zn muffin-tin potentials used here are based on those used earlier in Refs. 5 and 6. (See the appendix for a summary of the atomic potentials.) Using the examples of Cu_xNi_{1-x} and Cu_xZn_{1-x}, a comparison of the new ATA and the CPA electronic spectra is also presented.

To make this paper self-contained, the relevant expressions for $\langle\rho(E)\rangle$ and $\langle\rho_{A(B)}(E)\rangle$ are now summarized. In this connection, we consider the equations

$$\langle\rho(E)\rangle^{\rm eff} = \rho_0(E) - \frac{1}{\pi N}\,\mathrm{Im}\sum_L\sum_{\vec{k}}\left[\left(\frac{x}{1-T_{00}^{\rm eff}(\tau_{\rm eff}^{-1}-\tau_A^{-1})}\frac{d\tau_A^{-1}}{dE}+\frac{y}{1-T_{00}^{\rm eff}(\tau_{\rm eff}^{-1}-\tau_B^{-1})}\frac{d\tau_B^{-1}}{dE}-\frac{dB_{\vec{k}}}{dE}\right)\left(\frac{1}{\tau_{\rm eff}^{-1}-B_{\vec{k}}}\right)\right]_{LL}$$

$$\equiv \sum_{\vec{k}}\langle\rho(\vec{k},E)\rangle^{\rm eff}\ , \tag{1}$$

$$\langle\rho_A(E)\rangle^{\rm eff} = \rho_0(E) - \frac{1}{\pi N}\,\mathrm{Im}\sum_L\sum_{\vec{k}}\left[\left(\frac{1}{1-T_{00}^{\rm eff}(\tau_{\rm eff}^{-1}-\tau_A^{-1})}\frac{d\tau_A^{-1}}{dE}-\frac{\tau_{\rm eff}^{-1}-\tau_B^{-1}}{x(\tau_A^{-1}-\tau_B^{-1})}\frac{dB_k}{dE}\right)\left(\frac{1}{\tau_{\rm eff}^{-1}-B_{\vec{k}}}\right)\right]_{LL}, \tag{2}$$

with $\langle\rho_B(E)\rangle^{\rm eff}$ obtained from Eq. (2) using interchanges $A \rightleftharpoons B$ and $x \rightleftharpoons y$. Here $\rho_0(E) \equiv (V/4\pi^2N)E^{1/2}$ is the free-electron density of states, with N denoting the number of atoms and V the volume of the crystal. $L \equiv (l,m)$ is a composite angular momentum index including both orbital and magnetic quantum numbers. $B_k(E)$ is the matrix of usual Korringa–Kohn–Rostoker (KKR) structure functions. τ_A, τ_B, and $\tau_{\rm eff}$, respectively, are the on-the-energy-shell matrix elements of A, B, and the effective atom scattering operators. These are related to the phase shifts $\delta_l^{A(B)}$ via the familiar equation

$$[\tau_{A(B)}(E)]_l = -E^{-1/2}\exp[i\delta_l^{A(B)}(E)]\sin\delta_l^{A(B)}(E)\,. \tag{3}$$

The quantities $T_{00}^{\rm eff}$ are defined by

$$T_{00}^{\rm eff} = \frac{1}{N}\sum_{\vec{k}}\left[\frac{1}{\tau_{\rm eff}^{-1}-B_{\vec{k}}(E)}\right], \tag{4}$$

which is implicitly a matrix equation in the angular momentum (L) space. The $\vec{k}$ summations in Eqs. (1), (2), and (4) only extend over the first Bril-

louin zone.

Equations (1) and (2) yield the densities of states in the ATA or the CPA depending upon the choice of the effective scattering matrix τ_{eff}. If $\tau_{\text{eff}} = \langle\tau\rangle$, where

$$\langle\tau\rangle = x\tau_A + y\tau_B , \tag{5}$$

then Eqs. (1) and (2) yield the ATA spectrum. (Note that in Ref. 4, these were referred to as ATA2.) If on the other hand, $\tau_{\text{eff}} = \tau_{\text{CP}}$, where τ_{CP} is determined as a solution of the CPA equation

$$\tau_{\text{CP}}^{-1} = x\tau_A^{-1} + y\tau_B^{-1} + (\tau_{\text{CP}}^{-1} - \tau_A^{-1})T_{00}^{\text{CP}}(\tau_{\text{CP}}^{-1} - \tau_B^{-1}) , \tag{6}$$

then Eqs. (1) and (2) yield the CPA spectrum.[7]

The structure in the spectral function $\langle\rho(\vec{k},E)\rangle^{\text{eff}}$ in Eq. (1) arises from complex zeros of the equation

$$\|\tau_{\text{eff}}^{-1} - B_{\vec{k}}(E)\| = 0 \tag{7}$$

and also from those of

$$\|1 - T_{00}^{\text{eff}}(\tau_{\text{eff}}^{-1} - \tau_{A(B)}^{-1})\| = 0 . \tag{8}$$

Physically, the solutions of Eq. (7) give Bloch-type states in the average effective medium, and those of Eq. (8) give the impurity levels which result when an A or B atom is placed in the effective medium.

An outline of the this paper is presented as follows: Section II discusses the CPA effective scattering amplitudes τ_{CP}. A comparison of the CPA and ATA amplitudes reveals that the self-consistency in treating disorder has significant influence on the scattering matrices.

Section III presents and discusses the results pertaining to the Bloch spectral densities $\langle\rho(\vec{k},E)\rangle$, the complex energy levels, and the density of states. The structure in $\langle\rho(\vec{k},E)\rangle$ arising from the Bloch-type states and from virtually bound impurity-like states is considered. The Bloch-type complex energy solutions of Eq. (7) have been discussed previously in connection with the ATA,[4,5,8,9] but the importance of impurity-like contributions from Eq. (8) has been recognized only recently.[7]

The total and component densities of states in Cu_xNi_{1-x} and Cu_xZn_{1-x}, presented in Sec. III, show that the CPA and the new ATA spectra are in good agreement with regard to their positions and widths in energy over a wide range of alloy compositions. Aside from the greater overall smoothing of the CPA densities of states, the differences between the two approximations would largely appear to be confined to the details of the spectra.

Section IV discusses how effects of transfer of charge between the constituent atoms can be incorporated within the present framework. We show that Friedel's sum rule, which for present purposes amounts to the requirement that $dE_F(x)/dx \to 0$ for $x \to 0$ [$E_F(x)$ denotes the Fermi energy in an alloy with impurity concentration x][10] can be used to determine the impurity potential in dilute alloys. In general, however, one or another feature of the atomic potentials may be adjusted to force agreement between the theory and one particular experiment. The atomic potentials so determined can be used to test the theoretical predictions concerning other independent experiments. The aforementioned adjustments may be looked upon as a way of including dominant charge-transfer effects on atomic potentials semiempirically. Although our discussion proceeds with the example of Cu_xNi_{1-x}, the ideas presented in this section should be applicable more generally to transition- and noble-metal alloys.

II. EFFECTIVE SCATTERING AMPLITUDES

In discussing the effective scattering amplitudes, the function $\sin\delta_2(E)$ is plotted in Fig. 1.[11] The s and p phase shifts for the CuNi and CuZn systems of present interest vary slowly as a function of energy and are very similar in the ATA and CPA, and for this reason are not considered.[12] The position of the d resonance in a pure $A(B)$ crystal (which corresponds to $\delta_2 \to \pi/2$) appears as a peak in $\sin\delta_2$, making this a convenient function for presenting effective scattering amplitudes. Figure 1(a) for $Cu_{0.95}Ni_{0.05}$ shows that the peaks in the real as well as the imaginary parts of $\sin\delta_2$ arising from Ni impurities (marked by arrows) are shifted to higher energies by approximately 0.05 Ry in the CPA compared to the ATA.[13] We find such movements in the positions of the impurity peaks more generally in Cu rich as well as Ni rich Cu_xNi_{1-x}. This, however, as noted above, does not imply that corresponding differences will be present in the energy locations of the impurity spectra given by the ATA and CPA.

Figure 1(b) shows that the Zn d resonance around 0.1 Ry in $Cu_{0.7}Zn_{0.3}$ is much narrower than the Ni d resonance in Cu_xNi_{1-x}. Furthermore, the separation between the energy positions of Cu and Zn d levels is roughly twice as large as that between the Cu and Ni d levels. Both these factors tend to make the constituent d bands more independent of each other in Cu_xZn_{1-x} than in Cu_xNi_{1-x}. Indeed, the $\text{Re}(\sin\delta_2)$ ATA curve in Fig. 1(b) is seen to consist of two well-defined peaks, the lower of the two being characteristic of pure Zn and the upper of pure Cu. By contrast, the CPA phase shifts in Fig. 1(b) show much greater influence of Cu and Zn resonances on each other.

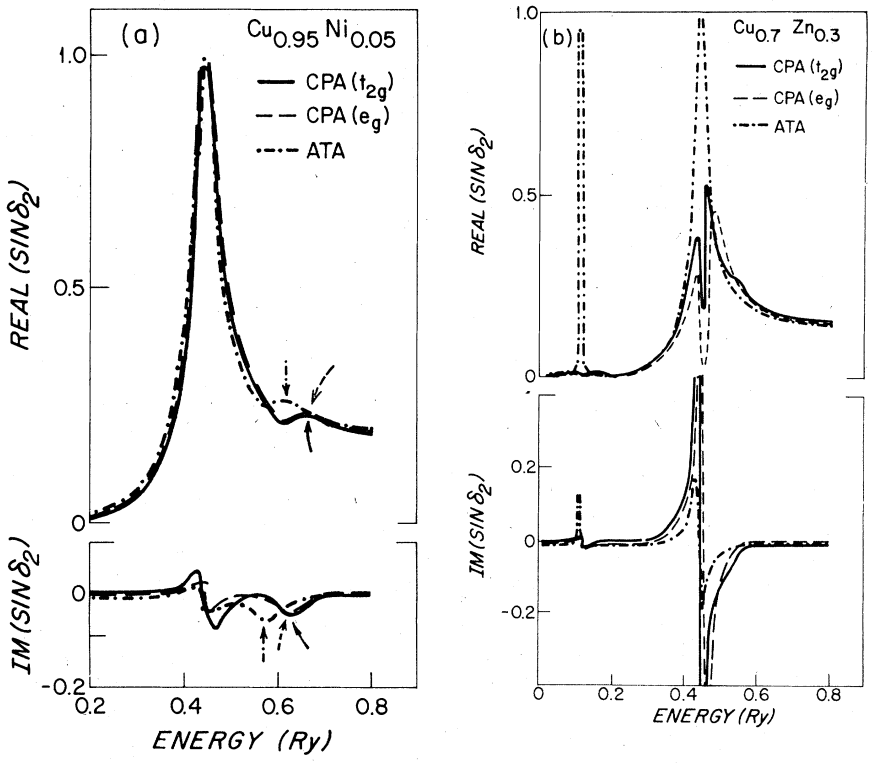

FIG. 1. Real and imaginary parts of $\sin\delta_2(E)$ in (a) $Cu_{0.95}Ni_{0.05}$ and (b) $Cu_{0.7}Zn_{0.3}$.[12] The arrows in (a) point out the bumps in the plotted curves in the energy region of the Ni impurity resonance in CPA (t_{2g}, solid; e_g, dashed) and ATA (dot-dashed).

Figure 1 also shows that the $\mathrm{Im}(\sin\delta_2)$ is generally larger in the CPA compared to the ATA. This leads to an increased overall damping of electronic states in the CPA, and will be seen more clearly in other connections below.

III. BLOCH SPECTRAL DENSITIES, COMPLEX ENERGY LEVELS, AND DENSITIES OF STATES

The Bloch spectral density $\langle\rho(\vec{k},E)\rangle$ and the representation of its structure in terms of the complex energy solutions of Eqs. (7) and (8) are taken up first.

Figure 2 gives $\langle\rho(\vec{k},E)\rangle$ as a function of E at the symmetry point Γ in the bcc Brillouin zone. The positions and half-widths of peaks in $\langle\rho(\vec{k},E)\rangle$ are seen to be respectively well correlated with the real and imaginary parts of the corresponding complex energy levels obtained from Eq. (7) for both the ATA and the CPA.[14] (These levels are marked along the horizontal axis in Fig. 2.) As noted above, solutions of Eq. (7) do not give all the structure in $\langle\rho(\vec{k},E)\rangle$; additional structure arises via Eq. (8). A striking example of this is the peak marked by an arrow in Fig. 2(a). Figure 3 shows $\langle\rho(\vec{k},E)\rangle$ at the symmetry point X, and once again

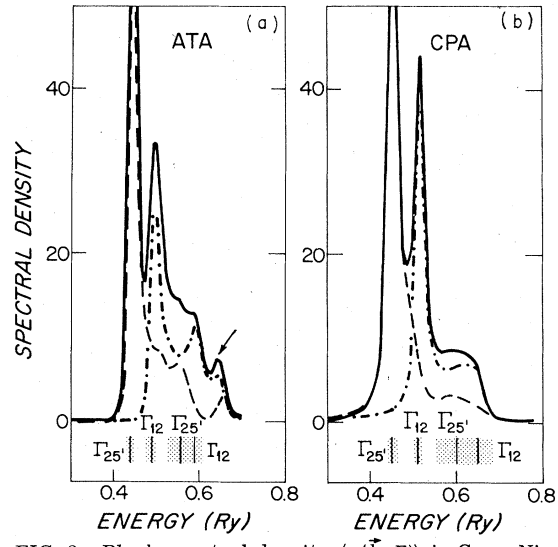

FIG. 2. Bloch spectral density $\langle\rho(\vec{k},E)\rangle$ in $Cu_{0.75}Ni_{0.25}$ at the point Γ in the Brillouin zone. The decomposition of $\langle\rho(\vec{k},E)\rangle$ into contributions of symmetry $\Gamma_{25'}$ (dashed) and Γ_{12} (dot-dashed) is shown. The complex energy solutions of Eq. (7) for $\vec{k}=(0,0,0)$ are marked along the energy axis. (Horizontal width of the shading around each level equals twice the imaginary part of the energy.) As discussed in the text, the peak marked by an arrow in (a) arises from complex energy solutions of Eq. (8).

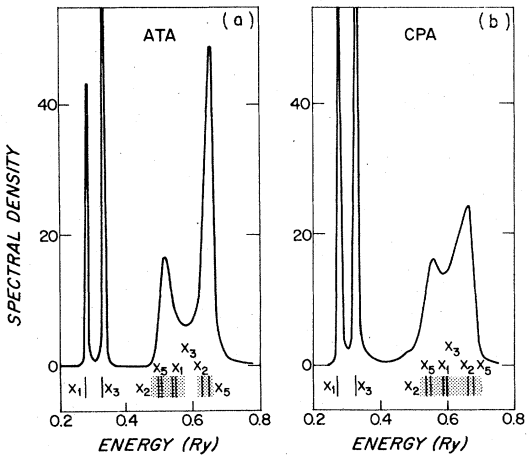

FIG. 3. Bloch spectral density $\langle \rho(\vec{k}, E) \rangle$ in $Cu_{0.75}Ni_{0.25}$ at the point X in the Brillouin zone. The complex energy solutions of Eq. (7) for $\vec{k} = (1, 0, 0)$ are marked along the energy axis. (See caption to Fig. 2 for meaning of the shading.)

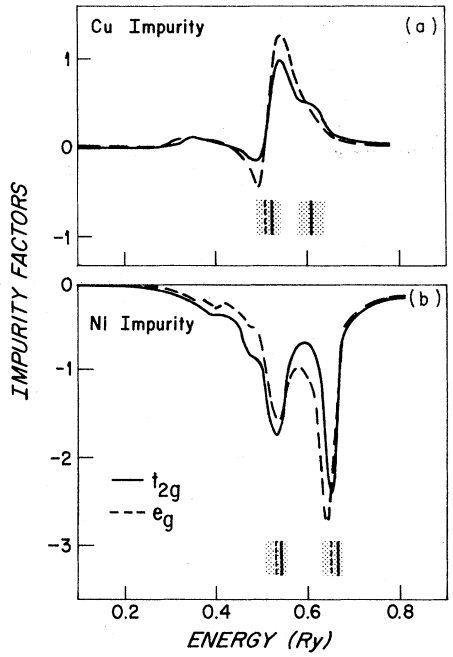

FIG. 4. Imaginary parts of the ATA impurity factors, $f^{\text{eff}}_{\text{Cu(Ni)}} \equiv 1/[1 - T^{\text{eff}}_{00}(\tau^{-1}_{\text{eff}} - \tau^{-1}_{\text{Cu(Ni)}})]$, with $\tau_{\text{eff}} = \langle \tau \rangle$ in $Cu_{0.75}Ni_{0.25}$ for (a) a Cu impurity and (b) a Ni impurity. (Real parts of $f^{\text{eff}}_{\text{Cu(Ni)}}$ are not shown for ease of drawing.) The corresponding complex energy solutions of Eq. (8) are marked along the horizontal axis. (See caption to Fig. 2 for meaning of the shading.) The curves as well as complex energy levels of t_{2g} symmetry are shown solid, while those of symmetry e_g are shown dashed.

the correlation between the complex bands and the spectral peaks is evident. We have carried out additional calculations at other points in the Brillouin zone and find that for sharp peaks (i.e., peaks with half widths at half maximum of less than approximately 0.01 Ry), this correlation holds very well. However, for values of half widths exceeding on the order of 0.05 Ry, the spectral peaks become rather poorly defined, and the calculation of the corresponding complex levels also becomes somewhat uncertain.

We now discuss solutions of Eq. (8). In the limit x (or y) $\to 0$, since $\tau_{\text{eff}} \to \tau_B$ (or τ_A), Eq. (8) gives real localized impurity levels for a single A (or B) atom placed in a perfect crystal of B (or A) atoms. In general, τ_{eff} corresponds to a complex effective potential and this equation yields complex solutions, which are physically akin to virtually bound impurity levels in the alloy. These corresponding d-like impurity levels can be obtained by solving for the complex zeros of the appropriate elements of the matrix $f^{\text{eff}}_{A(B)} \equiv 1 - T^{\text{eff}}_{00} \times (\tau^{-1}_{\text{eff}} - \tau^{-1}_{A(B)})$. Figures 4 and 5 show plots of what may be called impurity factors, i.e., $1/f^{\text{eff}}_{A(B)}$ (only the imaginary part is drawn) in $Cu_{0.75}Ni_{0.25}$ along with the corresponding complex energy solutions of Eq. (8). The location and widths of the peaks in the impurity factors in Figs. 4 and 5 are seen to be in good agreement with the real and imaginary parts of the corresponding complex levels.

Although the positions and widths of the spectral peaks are well represented by complex levels, these levels carry no information about the weights of the spectral peaks. The only qualitative statement that can be made in this regard is that if an energy level remains unsplit on alloying (e.g., levels such as $X_{4'}$, $L_{2'}$, and Γ_1 in Cu_xNi_{1-x}), then its total weight approximately remains unity, as in a perfect crystal. However, each of the levels

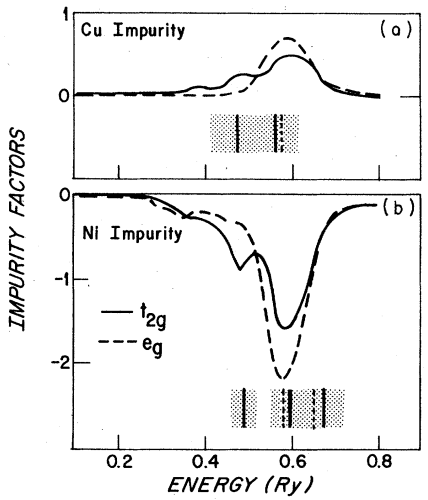

FIG. 5. Same as the caption to Fig. 4, except that this figure refers to the CPA, i.e., $\tau_{\text{eff}} \equiv \tau_{\text{CP}}$.

such as $\Gamma_{25'}$, Γ_{12}, X_2, and X_5 leads to two distinct levels of the same symmetry in the alloy, one of which may be viewed as having its origin in Cu-like d states and the other in Ni-like d states. In this case, the weights of the two levels in the alloy are roughly proportional to the concentrations x and $1-x$ of the Cu and Ni atoms.

In comparing the complex energy bands in $Cu_{0.75}Ni_{0.25}$, Fig. 6 shows that the center of gravity of the Ni d bands E_d^{Ni} [defined as $E_d^{Ni} \equiv \frac{3}{5}E(\Gamma_{25'}) + \frac{2}{5}E(\Gamma_{12})$, where $\Gamma_{25'}$ and Γ_{12} are the upper pair of levels in Fig. 6] lies at 0.57 Ry in the ATA, but that it has moved to 0.62 Ry in the CPA. This upward movement of the Ni d resonance in the CPA may be viewed as the result of increased $d-d$ repulsion of the Bloch-type d states given by τ_{CP} in comparison to $\langle\tau\rangle$.[13] If the impurity density of states $\langle\rho_{Ni}(E)\rangle$ were determined solely by the Bloch-type states in the alloy, Fig. 6 would imply that the Ni-impurity spectrum in the ATA would lie approximately 0.05 Ry lower in energy than the CPA. However, to obtain $\langle\rho_{Ni}(E)\rangle$ we must, in addition, consider contributions from solutions of Eq. (8). In this connection, Fig. 7 shows that for the Ni impurity the ATA impurity levels are localized in two groups around 0.66 and 0.53 Ry. Correspondingly, in this energy regime the CPA shows Ni-impurity levels in the vicinity of 0.67 and 0.58 Ry, and the situation is not as clear-cut as in the case of Bloch-type contributions. Nevertheless, as Fig. 8(a) shows, the final impurity spectrum $\langle\rho_{Ni}(E)\rangle$ in the ATA and CPA comes out in good agreement with regard to its location and width in energy in $Cu_{0.75}Ni_{0.25}$. In fact, Fig. 8(b) shows that $\langle\rho_{Ni}(E)\rangle$ in the two approximations is in even better agreement in $Cu_{0.95}Ni_{0.05}$. It is interesting to note that the Ni resonance for the ATA in the $\langle\rho(E)\rangle$ curve in this figure is not as well defined as in the corresponding CPA curve. This, however, in view of the $\langle\rho_{Ni}(E)\rangle$ and $\langle\rho_{Cu}(E)\rangle$ curves in Fig. 8(b) is not because the impurity spectrum is given poorly by the ATA, but arises from the fact that the edge of the Cu d band is somewhat broader in the ATA than in CPA in this alloy.

Figure 9 for $Cu_{0.7}Zn_{0.3}$ shows that although the Zn d band in the ATA is split into a two-peaked structure, its overall width and position is in accord with the corresponding CPA result. That the Zn d levels in CuZn are largely independent impurity levels, well separated from the host d bands, is also evident from Fig. 9. The CPA spectra in Figs. 8 and 9 are generally smoother than the ATA. This is to be anticipated in view of Figs. 6 and 7, which show that the CPA complex levels generally possess larger imaginary parts as compared to ATA. This appears to be a general feature of the CPA scatterers. It is note-

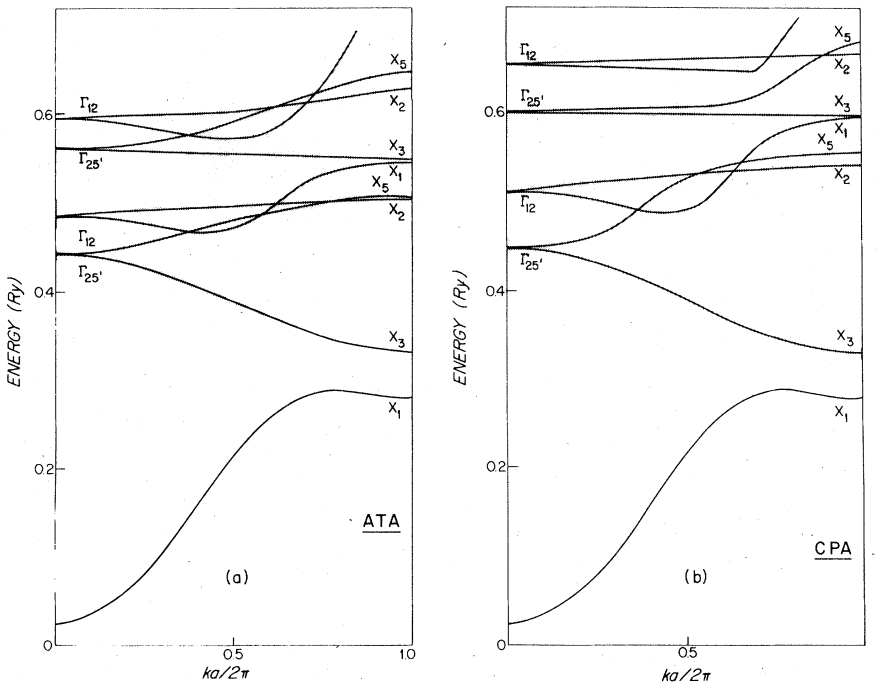

FIG. 6. Complex energy bands in $Cu_{0.75}Ni_{0.25}$ along the direction Δ in the Brillouin zone for (a) the ATA and (b) the CPA. The vertical length of shading around bands equals two times the imaginary part of the energy.

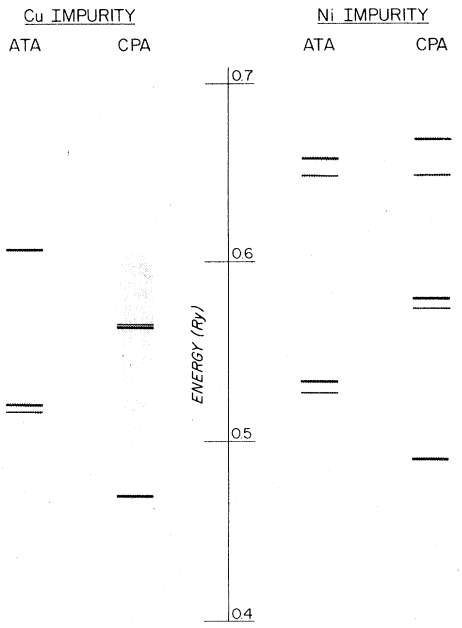

FIG. 7. Cu and Ni impurity level solutions of Eq. (8) in $Cu_{0.75}Ni_{0.25}$. Real parts of the levels of t_{2g} symmetry are shown as thick horizontal lines, while those of the e_g symmetry are given by lighter lines. The vertical length of the shading around each level equals two times the imaginary part of the energy.

worthy that the Cu d band for CPA in Fig. 8(a) is somewhat broader than for the ATA. This is also seen by comparing the corresponding complex levels in Fig. 6. A similar level of differences between the two approximations for the electronic spectrum in the vicinity of the band edges can be expected more generally.

In concluding this section we note that aspects of the spectral density or of the corresponding complex levels are accessible to current experiments on disordered alloys.[3] The Fermi-surface radii $\vec{k}(E_F)$ even in concentrated alloys can be measured by positron annihilation and Compton scattering experiments. With improvements in resolution, the positron annihilation experiments, especially in their present two-dimensional form, should also allow a determination of the smearing $\Delta\vec{k}(E_F)$ of the Fermi surface in $\vec{k}$ space. For dilute alloys, specific Fermi surface radii as well as the damping of the corresponding electronic states (directly related to the imaginary part of the complex levels) are observable via de Haas–van Alphen measurements. The changes in the energies of transitions between some of the complex levels have been monitored by optical experiments. Finally, the recent angularly resolved photoemission experiments, neglecting surface and matrix element effects, are related to the spectral density function $\langle\rho(\vec{k},E)\rangle$, whereas the usual photoemission experiments measure the average density of states $\langle\rho(E)\rangle$. The component densities of states are related to the soft x-ray emission profiles, using simplifying assumptions about matrix elements, relaxation effects, etc. The density of states at the Fermi energy has been estimated by the specific heat and magnetic susceptibility measurements.

IV. INTEGRATED DENSITIES OF STATES AND CHARGE TRANSFER

The integrals of the component densities of states $\langle\rho_A(E)\rangle$ and $\langle\rho_B(E)\rangle$ up to the Fermi energy E_F determine the total charges Q_A and Q_B associated with A and B atoms and allow the discussion of charge transfer between these atoms. Figure 10 shows the magnitude of charge transferred to a Cu site in $Cu_{0.75}Ni_{0.25}$ as a function of the shift ΔE_d^{Ni} in the position of the Ni d resonance. The agreement between the ATA and the CPA curves in this figure is seen to be reasonable. For $\Delta E_d^{Ni}=0$, $\Delta Q_{Cu}=-0.03$ electrons per atom spin, the negative sign meaning that charge is depleted from Cu sites. (Owing to charge neutrality of the average alloy, $x\Delta Q_{Cu}+(1-x)\Delta Q_{Ni}=0$, and hence the corresponding value of $\Delta Q_{Ni}=-[x/(1-x)]\times\Delta Q_{Cu}$.) As the Ni d resonance is moved to higher energy (i.e., ΔE_d^{Ni} increases), Fig. 10 shows the expected increase in ΔQ_{Cu}. In fact, for $\Delta E_d^{Ni}=0.1$ Ry there is a net depletion of charge from Ni sites in the alloy. It is clear that, if the quantity ΔQ_{Cu} (or ΔQ_{Ni}) is known from some experiment (e.g., Knight-shift or isomer-shift measurements), then the position of the Ni d resonance can be determined by treating it as an adjustable parameter.[15] So far we have assumed that ΔQ_A (or ΔQ_B) is known from an experiment. We emphasize, however, that this is not essential. In Cu_xZn_{1-x} in Ref. 5, for example, position of the Cu d resonance was obtained by requiring agreement between the theoretically predicted and experimentally measured composition dependence of the energy of the edge in optical absorption. [In this case, the theory would *predict* the value of ΔQ_{Cu} (and ΔQ_{Zn}) in the alloy.] The important point is that once the nature of the adjustable parameter is chosen, its value is determined unambiguously via an appropriate experimental measurement. The constituent atomic potentials so obtained can then be used to make predictions about other aspects of the alloy electronic spectrum.

For dilute alloys, the impurity potential can be determined by using arguments based on Friedel's sum rule. Our present interest is in its implica-

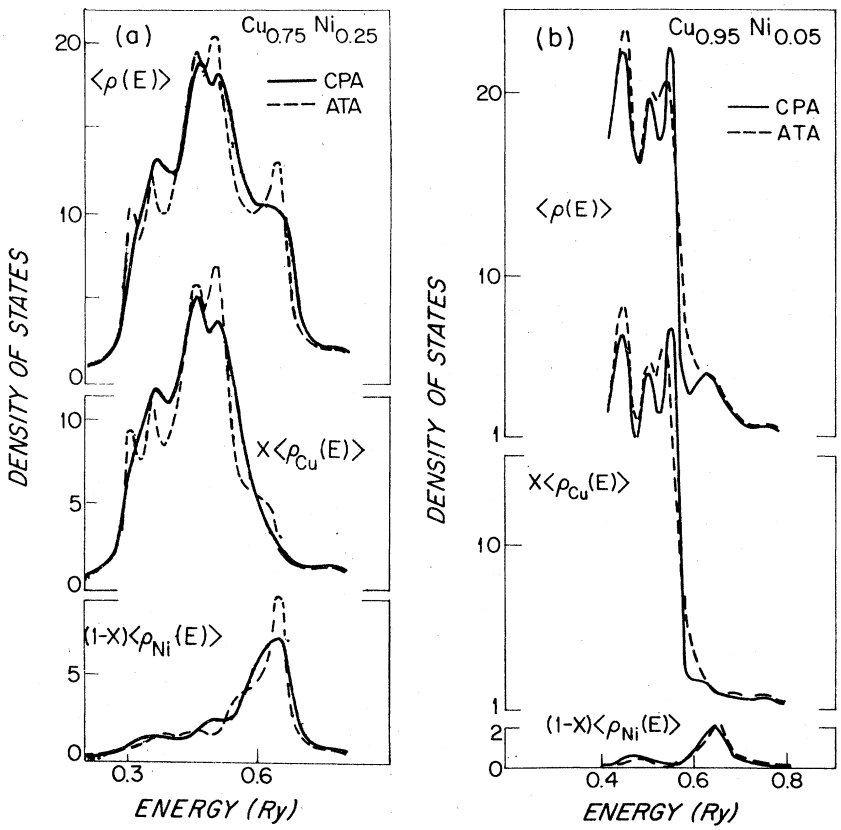

FIG. 8. CPA and ATA density of states $\langle\rho(E)\rangle$ and the weighted A and B component densities of states $x\,\langle\rho_A(E)\rangle$ and $(1-x)\langle\rho_B(E)\rangle$ in Cu_xNi_{1-x} for (a) $x=0.75$ and (b) $x=0.95$. [Note that $x\,\langle\rho_A(E)\rangle+(1-x)\langle\rho_B(E)\rangle=\langle\rho(E)\rangle$.]

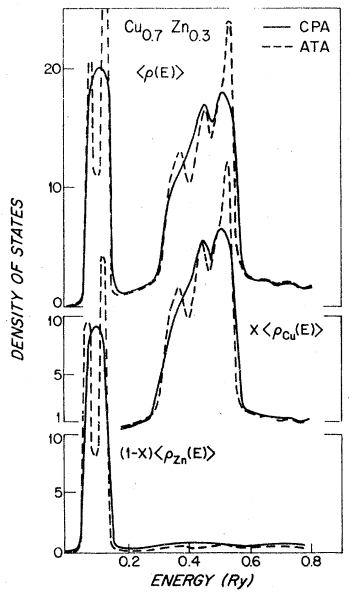

FIG. 9. Same as the caption to Fig. 8, except that this figure is for Cu_xZn_{1-x} with $x=0.70$.

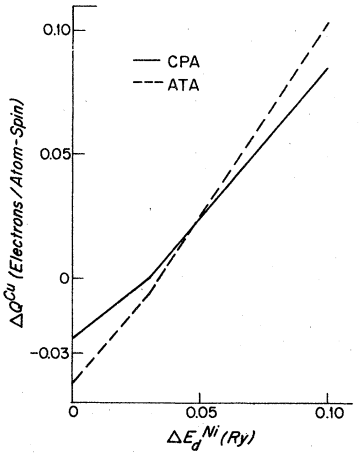

FIG. 10. Magnitude of the charge ΔQ^{Cu} transferred to a Cu atom in $Cu_{0.75}Ni_{0.25}$, as a function of the shift ΔE_d^{Ni} in the position of the Ni d resonance. $\Delta E_d^{Ni}=0$ corresponds to the Ni potential used in the ATA work of Ref. 6 and $\Delta Q^{Cu(Ni)}\equiv\int_{-\infty}^{E_F} dE\,\langle\rho_{Cu(Ni)}(E)\rangle - Z_{Cu(Ni)}$, where $Z_{Cu(Ni)}$ denotes the number of electrons per atom in a perfect Cu(Ni) crystal.

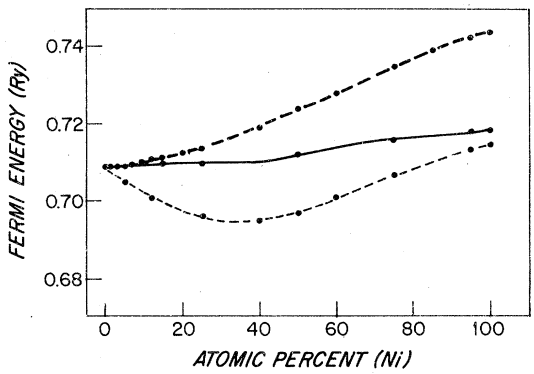

FIG. 11. Variation of the CPA Fermi energy in Cu_xNi_{1-x} as a function of the Ni concentration for three different Ni potentials. The light-dashed (lowest) curve is for the Ni potential used in the ATA work of Ref. 6, whereas the heavy-dashed (uppermost) curve employs a potential in which the Ni d resonance has been shifted upwards by $\Delta E_d^{Ni} = 0.03$ Ry. The solid curve corresponds to a weakly concentration dependent shift, $\Delta E_d^{Ni}(x) \equiv 0.03x + 0.01035(1-x)$ Ry.

tion that $dE_F/dx_{Ni(Cu)}$ must go to zero for the impurity concentration x_{Ni} (or x_{Cu})$\rightarrow 0$.[10] For $\Delta E_d^{Ni} = 0.03$, the heavy dashed curve in Fig. 11 shows that $dE_F/dx_{Ni} \rightarrow 0$ as $x_{Ni} \rightarrow 0$. By giving a small concentration dependence to ΔE_d^{Ni}, the solid curve in Fig. 11 [which corresponds to $\Delta E_d^{Ni}(x) \equiv 0.03x + 0.01035(1-x)$ Ry in Cu_xNi_{1-x}] is seen to be consistent with Friedel criteria in both the Cu- and the Ni-rich alloy. A reference to Fig. 10 shows that for $\Delta E_d^{Ni} = 0.03$, Cu and Ni atoms in $Cu_{0.75}Ni_{0.25}$ are essentially charge neutral. In fact, we have found that for the Ni potential corresponding to the solid curve in Fig. 11, the Cu and Ni atoms remain charge neutral to within approximately $\pm 0.01e$ over the entire composition range, in accord with the available experimental data on this alloy.[16] It suggests therefore that the Ni potential corresponding to the solid curve of Fig. 11 has, in some sense, incorporated complete self-consistency.

In concluding this section, we emphasize that the present discussion of Cu_xNi_{1-x} has largely been illustrative, and that similar semiempirical treatment of charge transfer and self-consistency effects should be useful more generally in transition- and noble-metal alloys.

ACKNOWLEDGMENTS

I am very grateful to Dr. P. N. Argyres, Dr. S. Berko, Dr. P. E. Mijnarends, Dr. R. Prasad, Dr. L. Schwartz, and Dr. G. M. Stocks for several important conversations. This work was supported in part by the National Science Foundation.

APPENDIX: DETAILS OF THE Cu, Ni, and Zn MUFFIN-TIN POTENTIALS

As already noted in the introduction the Cu, Ni, and Zn muffin-tin potentials used in this paper are based on those used in the earlier ATA work on Cu_xNi_{1-x} and Cu_xZn_{1-x}. In particular, these potentials are l dependent and have been obtained by the renormalized atom technique.[17]

The Cu potential is the same as was used for several density of states calculations in Ref. 6. This potential was denoted by V_{II}^{Cu} in Ref. 6, and differs from another potential V_I^{Cu}, which was also used in the earlier work on CuNi and on CuZn. V_I^{Cu} and V_{II}^{Cu} differ only in that the Cu d band in V_{II}^{Cu} is moved to an energy of approximately 0.06 Ry higher than in V_I^{Cu}. This was done in Ref. 6, because V_{II}^{Cu} gives a better agreement with relevant experimental data pertaining to the placement of Cu d bands with respect to the Fermi energy in crystalline Cu.

The Ni potential, aside from minor differences, is the same as was used in the earlier CuNi ATA work.[6] The present paper, however, also uses several other Ni potentials, which differ from this basic potential only in that the position of the Ni d band is moved in order to change the relative placement of the Cu and Ni d bands in CuNi. As discussed in Sec. IV, such movements of the d bands allow dominant effects of charge transfer to be included in transition- and noble-metal alloys.

Finally, the Zn atomic potential corresponds to the neutral atom potential used in our earlier CuZn work,[5] except that the Zn d band has been moved to somewhat higher energies. All calculations in the present paper use the fcc lattice structure with the crystalline Cu lattice constant of 6.8309 a.u. and a muffin-tin zero of −0.83 414 Ry.

[1] R. J. Elliott, J. A. Krumhansl, and P. L. Leath, Rev. Mod. Phys. 46, 465 (1974).

[2] H. Ehrenreich and L. M. Schwartz, in *Solid State Physics*, edited by H. Ehrenreich, F. Seitz, and D. Turnbull (Academic, New York, 1976), Vol. 31.

[3] For a recent review of the experimental literature see D. L. Sellmeyer in *Solid State Physics*, edited by H. Ehrenreich, F. Seitz, and D. Turnbull (Academic,

New York, 1978).
[4]A. Bansil, Phys. Rev. B 20, 4025 (1979).
[5]A. Bansil, H. Ehrenreich, L. Schwartz, and R. E. Watson, Phys. Rev. B 9, 445 (1974).
[6]A. Bansil, L. Schwartz, and H. Ehrenreich, Phys. Rev. B 12, 2893 (1975).
[7]A. Bansil, Phys. Rev. Lett. 41, 1670 (1978).
[8]C. D. Gelatt, H. Ehrenreich, and J. A. Weiss, Phys. Rev. B 17, 1940 (1977).
[9]A. Bansil, S. Bessendorf, and L. Schwartz, Inst. Phys. Conf. Ser. 39, 493 (1978).
[10]E. A. Stern, Phys. Rev. Lett. 26, 1630 (1971).
[11]All calculations in this article employ $l \leq 2$ pure-atom phase shifts. The $\vec{k}$-space integrations were carried out using the 21 special direction set of Fehlner and Vosko [Can. J. Phys. 54, 2159 (1976)], although the 13-direction set of Bansil [Solid State Commun. 16, 885 (1975)] would be adequate. To enhance the efficiency of the computations, the $\vec{k}$- and E-dependent scheme of Williams, Janak, and Moruzzi [Phys. Rev. B 6, 4509 (1972)] was used for evaluating the KKR structure functions $B_{\vec{k}}(E)$ and their derivatives $dB_{\vec{k}}/dE$. Free-electron singularities corresponding to first 15 reciprocal lattice vectors were subtracted from $B_{\vec{k}}(E)$ and $dB_{\vec{k}}/dE$. The remaining smoother parts of these functions were fitted by a 4th-order polynomial in E, using a 13-center expansion in the first Brillouin zone. This scheme reproduces the pure Cu band structure with an accuracy of a few mRy in the energy range of present interest.
[12]Since phase shifts are undetermined to $\pm\pi$, $\sin\delta_2$ has been defined such that $\mathrm{Re}(\sin\delta_2)$ is positive.
[13]This difference was also noted by Stocks, Gyorffy, Guiuliano, and Ruggiri [J. Phys. F 7, 1859 (1977)].
[14]$\tau_{CP}(E)$ is required at complex energies for obtaining the CPA complex-energy levels. The necessary extension of $\tau_{CP}(E)$ into the complex-energy plane was carried out by using a local least-squares fit to $E^{l+1/2}\cot\delta_l^{CP}(E)$ for real E values.
[15]The relative placement of d resonances as an adjustable parameter would appear to be a natural choice in transition- and noble-metal alloys.
[16]W. Gudat and C. Kunz, Phys. Status. Solidi 52, 433 (1972); A. Wenger, G. Burri, and S. Steinemann, Phys. Lett. A34, 195 (1971); J. C. Love, F. E. Obenshain, and G. Czjzek, Phys. Rev. B 3, 2827 (1971).
[17]L. Hodges, R. E. Watson, and H. Ehrenreich, Phys. Rev. B 5, 3953 (1972).